ACS Medicinal Chemistry Letters

Letter

[18F]ZCDD083: a PFKFB3-targeted PET tracer for atherosclerotic plaque imaging

Carlo De Dominicis, Paola Perrotta, Sergio Dall'Angelo, Leonie Wyffels, Steven Staelens, G. R. Y. de Meyer, and Matteo Zanda

ACS Med. Chem. Lett., **Just Accepted Manuscript** • DOI: 10.1021/acsmedchemlett.9b00677 • Publication Date (Web): 19 Feb 2020

Just Accepted

is published by the American Chemical Society. 1155 Sixteenth Street N.W., Washington, DC 20036

TOC Graphic

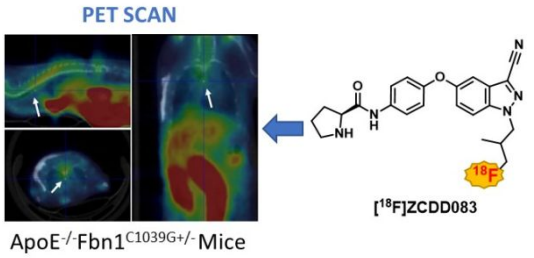

[^{18}F]ZCDD083: a PFKFB3-targeted PET tracer for atherosclerotic plaque imaging

Carlo De Dominicis,[1] Paola Perrotta,[2] Sergio Dall'Angelo,[1] Leonie Wyffels,[3] Steven Staelens,[3,*]

G.R.Y. De Meyer,[2,*] Matteo Zanda,[1,4,†,*]

[1]Kosterlitz Centre for Therapeutics, University of Aberdeen, AB25 2ZD Foresterhill, Aberdeen (UK)

[2]Laboratory of Physiopharmacology, University of Antwerp (Belgium)

[3]Molecular Imaging Center Antwerp, University of Antwerp (Belgium)

[4]CNR-ICRM, via Mancinelli 7, 20131 Milan (Italy)

ABSTRACT: PFKFB3, a glycolysis-related enzyme upregulated in inflammatory conditions and angiogenesis, is an emerging target for diagnosis and therapy of atherosclerosis. The fluorinated phenoxindazole [^{18}F]**ZCDD083** was synthesised, radiolabelled in 17 ±5% radiochemical yield and >99% radiochemical purity, and formulated for pre-clinical PET/CT imaging in mice. *In vivo* stability analysis showed no significant metabolite formation. Biodistribution studies showed high blood pool activity and slow hepatobiliary clearance. Significant activity was detected in the lung 2 h post-injection (pi) (11.0 ±1.5 %ID/g), while at 6 h pi no pulmonary background was observed. *Ex vivo* autoradiography at 6 h pi showed significant high uptake of [^{18}F]**ZCDD083** in the arch region and brachiocephalic artery of atherosclerotic mice, and no uptake in control mice, matching plaques distribution seen by lipid staining along with PFKFB3 expression seen by immunofluorescent staining. *In vivo* PET scans showed higher aortic region uptake of [^{18}F]**ZCDD083** in atherosclerotic ApoE$^{-/-}$Fbn1$^{C1039G+/-}$ than in control mice (0.78 ± 0.05 vs 0.44 ± 0.09 %ID/g). [^{18}F]**ZCDD083** was detected in aortic arch and brachiocephalic artery of ApoE$^{-/-}$ (with moderate atherosclerosis) and ApoE$^{-/-}$Fbn1$^{C1039G+/-}$ (with severe, advanced atherosclerosis) mice, suggesting this tracer may be useful for the non-invasive detection of atherosclerotic plaques *in vivo*.

KEYWORDS: Atherosclerosis, Plaque, Fluorine, PET imaging, glycolysis, preclinical.

INTRODUCTION

Atherosclerosis is a pathological process characterised by progressive accumulation of lipids, inflammatory cells and connective tissue in the arterial wall.[1] This process, leading to the formation of the so-called "atherosclerotic plaques", is predominantly asymptomatic. However, the progression of the disease can cause progressive stenosis of arterial lumen, which can eventually result in ischaemic heart pain. Acute clinical events, such as myocardial infarction, stroke and unstable angina, are mainly associated with instability of plaques and formation of occlusive thrombi.[2]

The progression of atherosclerotic plaques is initially asymptomatic, characterised by the slow growth of "silent" stable plaques. However, plaque rupture is associated with unstable angina, acute myocardial infarction, and sudden cardiac death. Similarly, rupture of carotid artery plaque is associated with cerebral ischemic events.[3] The risk of thrombotic complications of atherosclerosis is mostly related to the instability of an atheroma rather than the size of the plaque.

Currently, cardiovascular medicine aims principally to identify atherosclerotic plaques prone to rupture, improve the risk stratification, monitor the disease progression, assess new anti-atherosclerotic therapies and promptly evaluate the efficacy of therapeutic treatment. PET imaging is non-invasive and has a great potential in this context, but there is a clear need for new targets and radiotracers for imaging unstable atherosclerotic plaque.[4,5]

The PFKFB3 enzyme is emerging as a new target for the *in vivo* assessment of atherosclerotic plaques.[6,7] PFKFB3 is a glycolysis-related enzyme upregulated in inflammatory and hypoxic conditions.[8,9] Several studies have shown a correlation between PFKFB3 and angiogenesis, which is a feature of vulnerable atherosclerotic plaques.[10,11,12,13] Here we describe the development of the ^{18}F-radiolabelled phenoxindazole compound **ZCDD083** as a PFKFB3-targeted PET radiotracer for imaging the atherosclerotic plaque *in vivo*.[14] **ZCDD083** is a close structural mimic of the potent inhibitor AZ68 (IC_{50}= 4nM), whose radiofluorination was deemed to be chemically viable and unlikely to affect the binding to PFKFB3.

RESULTS

Phenol intermediate **2** (Scheme 1) was synthesised from *N*-Boc-proline and *O*-Bn-4-aminophenol, which were coupled to afford compound **1** that was debenzylated by hydrogenation over Pd/C.

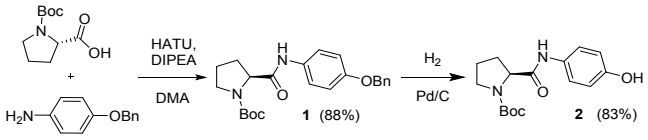

Scheme 1. Synthesis of phenol intermediate 2.

Indazole **4** (Scheme 2) was synthesised by NIS-promoted iodination of (2-amino)phenyl-acetonitrile, followed by indazole ring formation via Sandmeyer reaction and intramolecular ring closure of the diazonium salt formed from **3**.

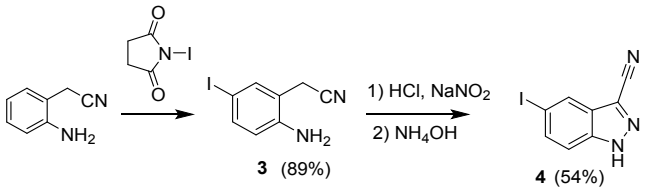

Scheme 2. Synthesis of indazole 4.

The radiofluorination precursor **7** (Scheme 3) was synthesized next. Commercial 2-methyl-1,3-propanediol was treated with tosyl chloride to give the mono tosylated derivative **5**, which was reacted with the indazole **4** via Mitsunobu reaction to give compound **6**. Ullmann-type coupling with phenol **2** afforded the target tosylated precursor **7**.

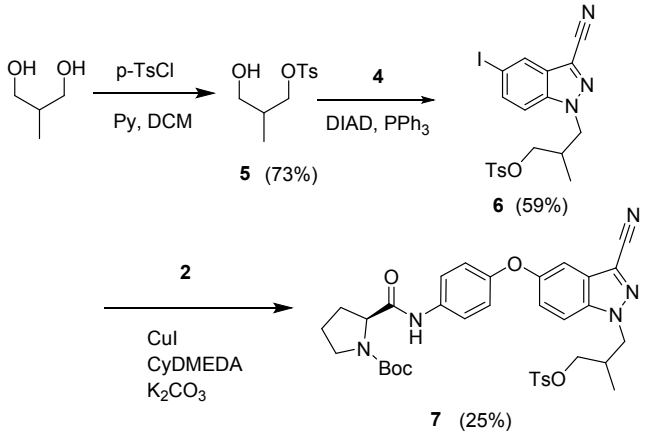

Scheme 3. Synthesis of radiofluorination precursor 7.

The 'cold' (e.g. non-radioactive) tracer **ZCDD083** (Scheme 4) was prepared from the indazole tosylate **6**, which was treated with TBAF to give the fluorinated compound **8**. The latter was subjected to the Ullmann coupling with **2** affording **9**, which was *N*-Boc-deprotected to afford the target molecule.

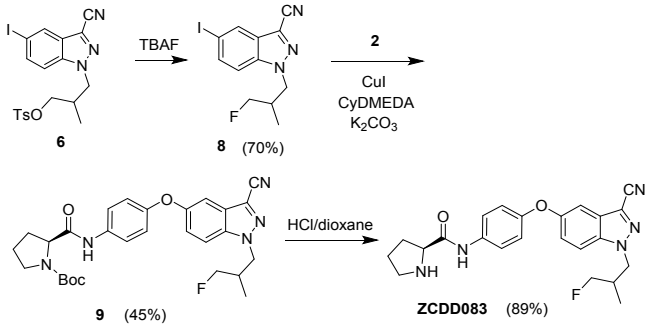

Scheme 4. Synthesis of 'cold' ZCDD083.

Starting from the tosylated precursor 7, [^{18}F]**ZCDD083** was radiosynthesised in a two-step synthesis (Scheme 5) using standard ^{18}F-fluoride chemistry, producing first the protected tracer **10** which was then treated with HCl in order to remove the N-Boc-protection.

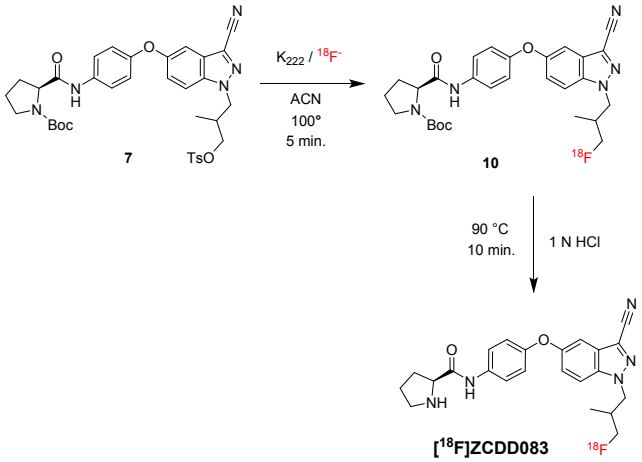

Scheme 5. Radiosynthesis of [^{18}F]ZCDD083.

[^{18}F]**ZCDD083** was obtained with a 17 ±5% radiochemical yield (decay-corrected to EOB) and the activity was in the range of 4.7-7.2 GBq (n = 7). The average time taken for synthesis, purification and formulation was 65 minutes. [^{18}F]**ZCDD083** was obtained with radiochemical purity >99%, specific activity >130 GBq/µmol, no impurities were detected in the UV chromatogram (**Fig. 1**) and no residual solvents other than ethanol (<10%) were detected (see **Fig. S4, Supporting Information**).

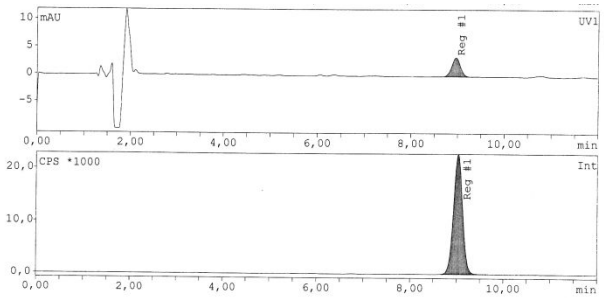

***Figure 1**. Chemical and radiochemical purity of [^{18}F]**ZCDD083** assessed by analytical RP-HPLC. No impurities were detected in the UV (top) and radioactive (bottom) chromatograms. Column: Phenomenex Luna C18 column (5 µm, 100 Å, 250 × 4.6 mm). Mobile phase: solvent A = H_2O + 0.1% TFA, solvent B = CH_3CN + 0.1% TFA; Isocratic method 40% B.*

A preliminary metabolite study was performed in healthy C57BL/6J mice (6 weeks old, female) to evaluate the *in vivo* plasma stability of [^{18}F]**ZCDD083**. The radio-HPLC analysis showed no significant metabolite formation within 6 h. The eluate from HPLC was collected in fractions and the radioactivity in each fraction was measured in a γ-counter. At 6 h pi, 78.9% ±1.2 of [^{18}F]**ZCDD083** was intact (see **Table S1** and **Fig. S5**, **Supporting Information**).

Ex vivo biodistribution of [^{18}F]**ZCDD083** was initially studied in healthy female C57BL/6J mice (**Table S2, Supp Information**). Measurement of radioactivity by γ-counter showed a high overall accumulation of [^{18}F]**ZCDD083** in tissues and organs within 2 h pi, as shown in **Fig. 2**. More specifically, high blood radioactivity was observed (7.2 ±2.2

%ID/g at 15 min pi, 5.5±1.6 %ID/g at 1 h pi, and 2.1±0.4 %ID/g at 2 h pi), revealing a slow clearance of [^{18}F]**ZCDD083** from blood pool. Also, high pulmonary uptake was found (34.7 ± 6.0 %ID/g at 15 min) with a slow washout from lungs (11.0 ± 1.5 %ID/g at 2 h. On the contrary, at 6 h pi the radioactivity in lungs and blood was significantly lower (5.5±3.9 %ID/g and 1.5±1.1 %ID/g respectively). Instead, at the late time point [^{18}F]**ZCDD083** had mostly accumulated in the excretory organs (*i.e.* 25.5 ± 3.8 %ID/g in small intestine and 47.9 ± 6.4 %ID/g in large intestine). Level of uptake in the liver and the intestines were significantly higher compared to the kidneys. Therefore, it can be concluded that [^{18}F]**ZCDD083** is predominantly cleared via the hepatobiliary system into the intestines and that the renal clearance is less significant.

Ex vivo biodistribution evaluation at 6 h pi was carried out also in atherosclerotic ApoE$^{-/-}$ mice (**Table S3, Supp Information**). A similar [^{18}F]**ZCDD083** biodistribution profile was observed in atherosclerotic ApoE$^{-/-}$ and control C57BL/6J mice. Pharmacokinetic studies in ApoE$^{-/-}$ atherosclerotic mice confirmed the plasma half-life of [^{18}F]**ZCDD083** (1.4 ±0.2 %ID/g in blood). Residual high radioactivity accumulation was observed in lungs (8.6 ± 1.9 %ID/g), whereas the maximal uptake was found in small and large intestine (40.6 ± 45.8 %ID/g and 35.6 ± 2.3 %ID/g respectively).

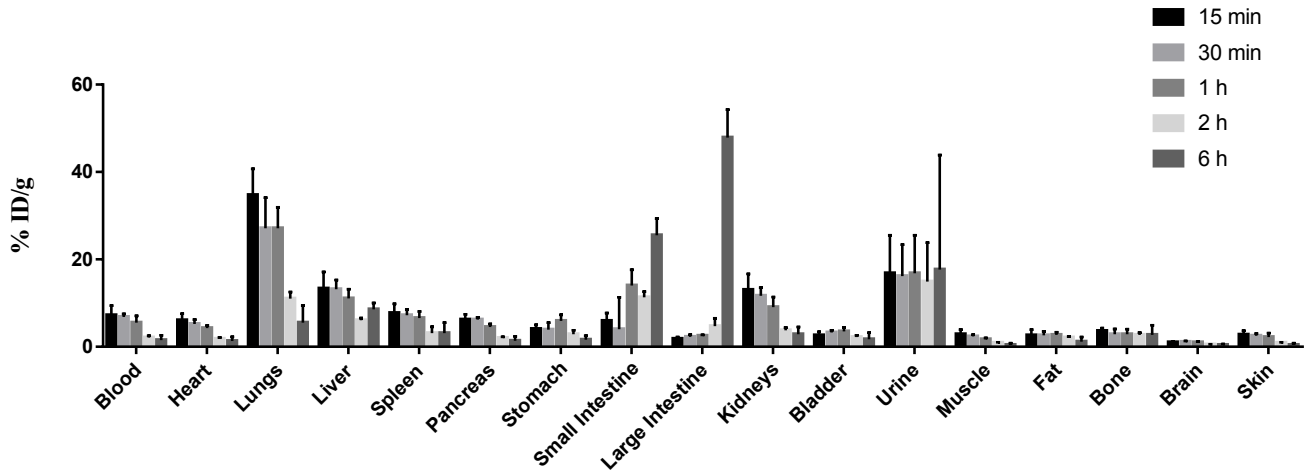

***Figure 2**. Ex vivo biodistribution of [^{18}F]**ZCDD083**. Slow blood clearance and high tracer uptake in the lungs were observed at earlier time points within 2 h pi. At 6 h pi [^{18}F]**ZCDD083** was mostly accumulated in the intestines.*

[^{18}F]**ZCDD083** PET imaging scans were performed using two different disease models (ApoE$^{-/-}$, with moderate atherosclerosis, and ApoE$^{-/-}$Fbn1$^{C1039G+/-}$, with severe advanced atherosclerosis, both female) and aged-matched wild type C57BL/6J female mice as controls. Representative PET/CT scans of ApoE-/-Fbn1$^{C1039G+/-}$ mice are shown in **Fig. 3**. Spherical ROIs were drawn manually over each aortic arch and ascending aorta using the axial view of CT images. The [^{18}F]**ZCDD083** signal was then quantified as SUV_{mean} (mean Standardized Uptake Values). Tracer uptake was different in ApoE$^{-/-}$Fbn1$^{C1039G+/-}$ (SUV 0.78 ± 0.05), ApoE$^{-/-}$ (SUV 0.55 ± 0.06) and C57BL/6J mice (SUV 0.44 ± 0.09), with significant difference between first and latter series, as shown in **Fig. 4**.

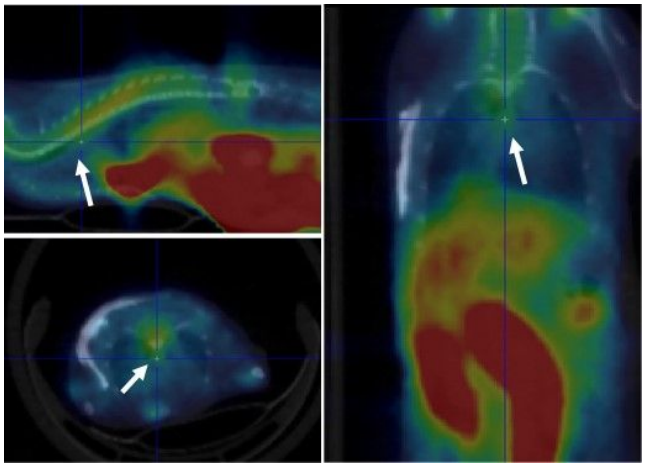

***Figure 3**. Representative axial, sagittal and coronal views of PET/CT images of ApoE-/-Fbn1C1039G+/-acquired at 6 h after injection of [^{18}F]**ZCDD083**. Radioactive signal in aorta (white arrows) was observed.*

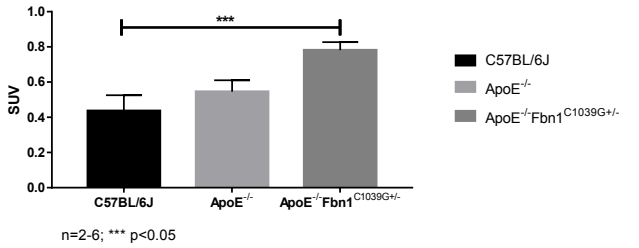

Figure 4**. Comparison of SUV measurements in C57BL/6J (n = 6), ApoE-/- (n = 6) and ApoE−/−Fbn1C1039G+/− mice (n = 2). All values are given as mean ± SD. One-way ANOVA was performed to test for difference between groups. One ApoE−/−Fbn1C1039G+/− mouse was excluded from the analysis because of a PET image acquisition technicality. (p = 0.0006, one-way ANOVA followed by Brown-Forsythe test).*

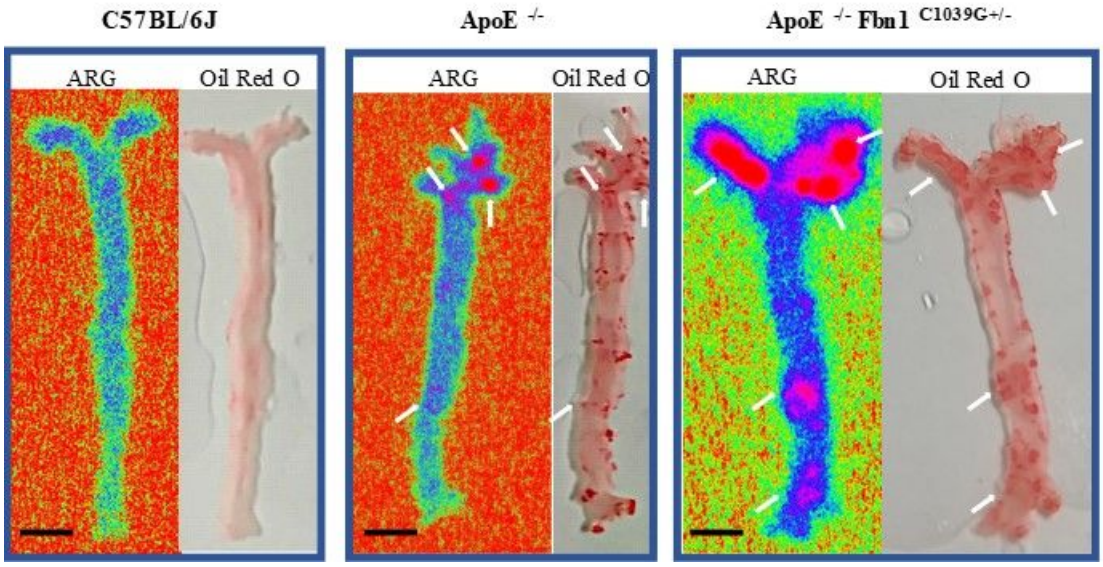

***Figure 5**. [18F]**ZCDD083** aortic uptake vs plaque distribution. Ex vivo autoradiography (left part of the insets) and fat staining using Oil-red O (right part of the insets) of longitudinally opened aortas at 6h post injection of [18F]**ZCDD083** in C57BL/6J control mice (left) compared to atherosclerotic mice (ApoE-/- and ApoE-/-Fbn1C1039G+/-, centre and right respectively, as indicated by the white arrows. [18F]**ZCDD083** uptake colocalises with atherosclerotic plaques. Scale bar = 1 cm.*

At the end of the PET imaging scans, three mice of C57BL/6J, ApoE$^{-/-}$ and ApoE$^{-/-}$Fbn1$^{C1039G+/-}$ were sacrificed and the aorta was harvested for Red Oil O staining and autoradiography (ARG). The *ex vivo* distribution of atherosclerotic plaques within the aorta was assessed by Red Oil O staining, whereas the accumulation of [^{18}F]**ZCDD083** was assessed by autoradiography of the in vivo injected [^{18}F]**ZCDD083**. This aforementioned Red Oil O staining and ex *vivo* autoradiography were performed on the same aortic specimens in order to visually compare fat-stained areas and tracer distribution within the aorta (**Fig. 5**).

Aortas from C57BL/6J control mice did not show focal lipid stained areas and radioactivity signal. Conversely, atherosclerotic plaques were found in ApoE$^{-/-}$ mice, especially in the aortic arch, proximal aorta and brachiocephalic aorta. The Oil Red O staining showed also a low plaque load in the thoracic descending aorta of the ApoE$^{-/-}$ strain. The ARG of the same specimen showed that the tracer accumulation within the aorta matched exactly with the distribution of atherosclerotic lesions. More specifically, the radioactivity was accumulated mostly in the aortic arch and in the branches. In these regions, [^{18}F]**ZCDD083** uptake was significantly higher in ApoE$^{-/-}$ (0.022 ± 0.004 %ID/µL) than control mice (0.011 ± 0.003 %ID/µL) (p = 0.0378, unpaired t test).

The correlation between plaques and tracer uptake was also consistent using ApoE$^{-/-}$Fbn1$^{C1039G+/-}$ mice with higher plaque load than the ApoE$^{-/-}$ strain.[27] The comparison of corresponding *en face* lipid staining and ARG signals demonstrated a high correlation of fat-stained areas and radioactivity distribution. ApoE$^{-/-}$Fbn1$^{C1039G+/-}$ mice showed more extended atherosclerotic lesions in the arch region, brachiocephalic artery along with thoracic descending aorta. [^{18}F]**ZCDD083** was, indeed, detected in the same areas along the aorta.

Aortic specimens of C57BL/6J and ApoE$^{-/-}$ (*n* = 3/ each group) were used for further histological analysis after PET

imaging scans. Longitudinal sections of aortic arch and right common carotid artery as well as cross sections of brachiocephalic aorta and proximal aorta were stained with haematoxylin and eosin (H&E) to visualise atherosclerotic plaques and lesion morphology. Aortas of healthy mice did not show atherosclerosis, whereas ApoE$^{-/-}$ mice showed fibrous/atheromatous plaques and some small calcifications. The H&E staining confirmed atherosclerotic disease especially in brachiocephalic artery, proximal aorta and aortic arch. The immunohistochemistry of ApoE$^{-/-}$ aortic arch sections, revealed that the enzyme target PFKFB3 is overexpressed inside atherosclerotic plaques (see **Fig. S6, Supporting Information**).

The comparison among brachiocephalic arteries of atherosclerotic and control mice showed that PFKFB3 was highly expressed within atherosclerotic plaques, whereas in normal vessels PFKFB3 is present just in a basal level along the arterial wall (**Fig. 6**).

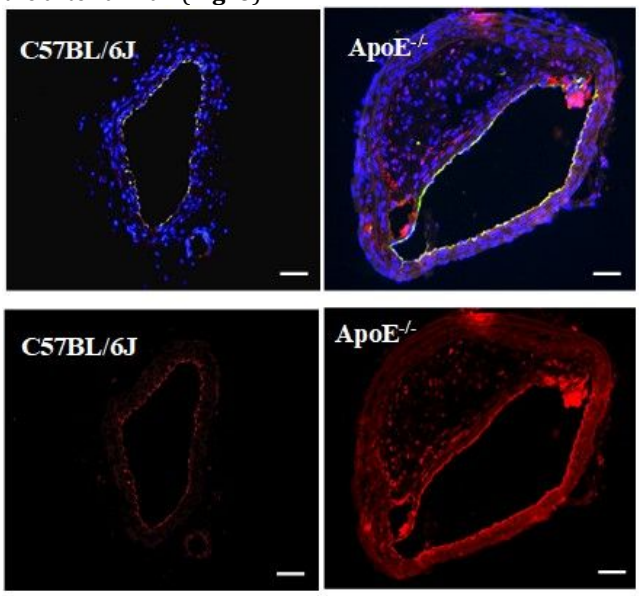

***Figure 6**. Immunohistochemistry of murine brachiocephalic arteries. Upper panels = immunofluorescent staining for von Willebrand factor to detect endothelial cells (green) and PFKFB3 (red). Counter-staining with DAPI to detect nuclei (blue). Lower panels = PFKFB3 staining (red). ApoE$^{-/-}$ mice exhibit high expression level of PFKFB3 enzyme in contrast to C57BL/6J controls. Scale bar = 50 µm.*

DISCUSSION

Atherosclerosis is responsible for the majority of acute cardiovascular events. Specifically, rupture of atherosclerotic plaques and consequent thrombosis remains the largest underlying cause of cardio- and cerebrovascular death. Despite extraordinary advances in the understanding of the pathophysiology of atherosclerosis, both the diagnosis and treatment of the disease still present limitations. Currently, the main challenge in cardiovascular medicine is to identify patients who are at risk of coronary plaque rupture and subsequent heart attack or stroke originating from carotid plaque depositions.[15] Among the cardiovascular imaging modalities used, coronary angiography has a wide clinical application but provides information only on vessel stenosis. Other imaging techniques, such as intravascular ultrasound (IVUS), optical coherence tomography (OCT) and near-infrared spectroscopy (NIRS), can provide only a limited plaque characterisation but, unfortunately, they are invasive and thus not useful for patient diagnosis and follow up.[16,17,18] Therefore, new non-invasive approaches to detect potentially unstable plaque are urgently needed.

In this context, PET imaging has great potential, since - compared to other molecular imaging modalities - it shows higher sensitivity allowing better visualisation of biological and biochemical processes involved in the development of atherosclerotic plaques.[19] [^{18}F]FDG (inflammation, approved for clinical use) and [^{18}F]NaF (micro-calcification) have been investigated in a clinical setting for detection and characterisation of atherosclerotic plaques in the major coronary arteries.[19,20]—However, new targets and radiotracers are currently being investigated preclinically for imaging atherosclerotic plaque.[21] Clinical studies showed that ^{18}F-FDG is useful to assess carotid artery stenosis in asymptomatic patients.[22,23] However, carotid artery imaging using ^{18}F-FDG PET is challenging due to (1) the low spatial resolution of PET (≈ 3 mm in human PET and 1.2 mm in rodent PET, using our setting), (2) cardiac motion and (3) myocardial spill over.[24] To address the latter limitation, new imaging targets and radiotracers having lower unspecific myocardial uptake are currently under investigation.[25]

The results above validate the PFKFB3 enzyme as an imaging target of atherosclerosis in two mouse models.[26,27] Firstly, we observed – via PET/ARG – an increased target engagement in cross sections of diseased aortas of atherosclerotic mice compared to those of healthy mice. Secondly, longitudinal sections of aortic arch specimens of ApoE$^{-/-}$ mice showed higher expression level of PFKFB3 enzyme within atherosclerotic plaques compared to normal vessel wall. Hence, all these results demonstrated the appropriateness and the specificity of the PFKFB3 target for the detection of atherosclerotic plaques.

The new PFKFB3-targeted tracer, [^{18}F]**ZCDD083** could be obtained in high radiochemical yields, activity concentrations and quality parameters. [^{18}F]**ZCDD083** demonstrated high *in vivo* metabolic stability and long circulation time in the blood. The slow clearance from the blood may be explained by the high hydrophobicity of [^{18}F]**ZCDD083**. Indeed, a $LogD_{7.4}$ of 3.6 was reported for the parent compound **AZ68**.[14] The correlation of high hydrophobicity with high binding to plasma proteins and prolonged circulation time in the blood is well known.[28] High binding to plasma proteins is documented for the compound **AZ26**[14] (chemically similar to **AZ68**) and might be valid also for our tracer [^{18}F]**ZCDD083**. This may likely explain the slow tracer clearance. Also, the excretion route is usually related to lipophilicity, as lipophilic compounds are generally cleared via the hepatobiliary system. This is in accordance with our *ex vivo* biodistribution results which showed a predominant excretion from the liver to the intestines. We also noticed a high uptake in the lung. However, it is not clear whether this high uptake in the lung is due to nonspecific binding (due to the high [^{18}F]**ZCDD083** lipophilicity) or somehow correlated with PFKFB3 tissue distribution. In 2003, Minchenko *et al.* studied the *in vivo* expression of the PFKFB enzyme family and its response to hypoxia, disclosing that lungs exhibit high basal level of

PFKFB3 mRNA.[29] Furthermore, it was recently shown that lung endothelial cells express high levels of glucose metabolic enzymes, such as PFKFB3.[30] Finally, the proteome analysis reported in the Human Protein Atlas shows that lung, stomach and placenta have the highest PFKFB3 expression among all tissues considered.[31]

Our PET imaging studies showed significantly increased signals in the aorta of ApoE$^{-/-}$ (+25%) and ApoE$^{-/-}$Fbn1$^{C1039G+/-}$ (+79%) compared to C57BL/6J mice. This is in accordance with the higher plaque burden in ApoE$^{-/-}$Fbn1$^{C1039G+/-}$ mice compared to ApoE$^{-/-}$ mice.[27] Moreover, these results were supported by aortic autoradiography which showed a 2-fold increased uptake in the aortic arch of ApoE$^{-/-}$ compared to WT mice. The autoradiographic signal in ApoE$^{-/-}$Fbn1$^{C1039G+/-}$ was considerably higher too. The increment in uptake is clearly correlated with the increment in plaque load, as confirmed by histological evaluation. Indeed, the highest uptake was found in ApoE$^{-/-}$Fbn1$^{C1039G+/-}$ at an advanced stage of the disease and high level of plaques in the aortic arch along with the thoracic aorta.

Unfortunately, despite the higher uptake, the [^{18}F]**ZCDD083** signal in these small sized atherosclerotic plaques was affected by partial volume effect and, due to the limited spatial resolution of PET,[32] no "hotspots" could be detected in the *in vivo* imaging studies. Indeed, the vessel wall in mouse aorta is usually 30-80 μm, whereas the resolution in rodent PET imaging is ~1,2 mm.

The specificity of the tracer accumulation at the target structure (*i.e.* atherosclerotic plaque) was demonstrated by the combination of *ex vivo* autoradiography with *en face* Oil Red O staining of the same aortic specimens. Indeed, we observed co-localisation of [^{18}F]**ZCDD083** signal with plaque distribution along the aorta. These cross studies, involving C57BL/6J, ApoE$^{-/-}$ and ApoE$^{-/-}$Fbn1$^{C1039G+/-}$ demonstrated high sensitivity of [^{18}F]**ZCDD083** to detect atherosclerotic plaques, whereas little signal was detected in normal vessel or outside atherosclerotic lesions. These stained areas exhibited a higher tracer accumulation. Hence, the [^{18}F]**ZCDD083** uptake was clearly correlated with plaque distribution as well as with the progression of the disease.

CONCLUSION

In summary, we efficiently radio-synthesized the novel PET tracer [^{18}F]**ZCDD083** which targets the PFKFB3enzyme. Using *in vivo* and *ex vivo* studies, we characterized and validated [^{18}F]**ZCDD083**, demonstrating its ability to detect atherosclerotic plaques. This tracer may represent a promising tool for the non-invasive diagnosis and follow-up of atherosclerotic plaques prone to rupture, which in turn could help improving risk stratification and evaluation of the efficacy of anti-atherosclerotic therapies.

ASSOCIATED CONTENT

Supporting Information

Experimental procedures for the synthesis of all the compounds described in this paper, radiochemistry procedures for [^{18}F]**ZCDD083**, animal models, in vivo metabolite analysis, ex vivo biodistribution, PET/CT imaging, autoradiography and histology. Copies of the ^{1}H, ^{19}F and ^{13}C NMR spectra of all the new compounds.

The Supporting Information is available free of charge on the ACS Publications website.

AUTHOR INFORMATION

Corresponding Author

*Phone: +44 01509564129. E-mail: m.zanda@lboro.ac.uk

*Phone : +3232652737. E-mail: guido.demeyer@uantwerpen.be

*Phone : +3232652820. E-mail: steven.staelens@uantwerpen.be

Present Addresses

†Centre for Sensing and Imaging Science, Loughborough University, LE11 3TU Loughborough (UK)

Author Contributions

CDD performed and co-designed all the experiments, contributed to writing the manuscript. SDA, and LW designed and performed radiochemistry experiments, reviewed the manuscript. SS designed in vivo experiments and reviewed the manuscript. GDM designed biology experiments and reviewed the manuscript. MZ designed the experiments and wrote the manuscript.

Funding Sources

We thank the European Union's Horizon 2020 research and innovation programme under the Marie Skłodowska-Curie ITN-European Joint Doctorate MOGLYNET (grant agreement No. 675527).

Notes

The authors declare no competing financial interest.

ACKNOWLEDGMENT

We are grateful to Rita Van Den Bossche, University of Antwerp, for performing the immunohistochemical stainings.

ABBREVIATIONS

CCR2, CC chemokine receptor 2; CCL2, CC chemokine ligand 2; CCR5, CC chemokine receptor 5; TLC, thin layer chromatography.

REFERENCES

(1) Lusis, A. J. Atherosclerosis. *Nature* **2000**, *407* (6801), 233–241. https://doi.org/10.1038/35025203.

(2) Ross, R. Atherosclerosis — An Inflammatory Disease. *N. Engl. J. Med.* **1999**, *340* (2), 115–126. https://doi.org/10.1056/NEJM199901143400207.

(3) Spagnoli, L. G.; Bonanno, E.; Sangiorgi, G.; Mauriello, A. Role of Inflammation in Atherosclerosis. *J. Nucl. Med.* **2007**, *48* (11), 1800–1815. https://doi.org/10.2967/jnumed.107.038661.

(4) Tawakol, A.; Finn, A. V. Imaging Inflammatory Changes in Atherosclerosis. *JACC Cardiovasc. Imaging* **2011**, *4* (10), 1119–1122. https://doi.org/10.1016/j.jcmg.2011.09.001.

(5) Rudd James H.F.; Hyafil Fabien; Fayad Zahi A. Inflammation Imaging in Atherosclerosis. *Arterioscler.*

Thromb. Vasc. Biol. **2009**, *29* (7), 1009–1016. https://doi.org/10.1161/ATVBAHA.108.165563.

(6) Van Schaftingen, E.; Jett, M. F.; Hue, L.; Hers, H. G. Control of Liver 6-Phosphofructokinase by Fructose 2,6-Bisphosphate and Other Effectors. *Proc. Natl. Acad. Sci. U. S. A.* **1981**, *78* (6), 3483–3486.

(7) Okar, D. A.; Lange, A. J. Fructose-2,6-Bisphosphate and Control of Carbohydrate Metabolism in Eukaryotes. *BioFactors* **1999**, *10* (1), 1–14. https://doi.org/10.1002/biof.5520100101.

(8) Pober, J. S.; Sessa, W. C. Evolving Functions of Endothelial Cells in Inflammation. *Nat. Rev. Immunol.* **2007**, *7* (10), 803–815. https://doi.org/10.1038/nri2171.

(9) Zhang, R.; Li, R.; Liu, Y.; Li, L.; Tang, Y. The Glycolytic Enzyme PFKFB3 Controls TNF-α-Induced Endothelial Proinflammatory Responses. *Inflammation* **2019**, *42* (1), 146–155. https://doi.org/10.1007/s10753-018-0880-x.

(10) Tawakol, A.; Singh, P.; Mojena, M.; Pimentel-Santillana, M.; Emami, H.; MacNabb, M.; Rudd, J. H. F.; Narula, J.; Enriquez, J. A.; Través, P. G.; et al. HIF-1α and PFKFB3 Mediate a Tight Relationship between pro-Inflammatory Activation and Anaerobic Metabolism in Atherosclerotic Macrophages. *Arterioscler. Thromb. Vasc. Biol.* **2015**, *35* (6), 1463–1471. https://doi.org/10.1161/ATVBAHA.115.305551.

(11) Parathath, S.; Yang, Y.; Mick, S.; Fisher, E. A. Hypoxia in Murine Atherosclerotic Plaques and Its Adverse Effects on Macrophages. *Trends Cardiovasc. Med.* **2013**, *23* (3), 80–84. https://doi.org/10.1016/j.tcm.2012.09.004.

(12) Sluimer, J. C.; Daemen, M. J. Novel Concepts in Atherogenesis: Angiogenesis and Hypoxia in Atherosclerosis. *J. Pathol.* **2009**, *218* (1), 7–29. https://doi.org/10.1002/path.2518.

(13) Perrotta, P.; Emini Veseli, B.; Van der Veken, B.; Roth, L.; Martinet, W.; De Meyer, G. R. Y. Pharmacological Strategies to Inhibit Intra-Plaque Angiogenesis in Atherosclerosis. *Vascul. Pharmacol.* **2019**, *112*, 72–78. https://doi.org/10.1016/j.vph.2018.06.014.

(14) Boyd, S.; Brookfield, J. L.; Critchlow, S. E.; Cumming, I. A.; Curtis, N. J.; Debreczeni, J.; Degorce, S. L.; Donald, C.; Evans, N. J.; Groombridge, S.; et al. Structure-Based Design of Potent and Selective Inhibitors of the Metabolic Kinase PFKFB3. *J. Med. Chem.* **2015**, *58* (8), 3611–3625. https://doi.org/10.1021/acs.jmedchem.5b00352.

(15) Qureshi, W. T.; Rana, J. S.; Yeboah, J.; bin Nasir, U.; Al-Mallah, M. H. Risk Stratification for Primary Prevention of Coronary Artery Disease: Roles of C-Reactive Protein and Coronary Artery Calcium. *Curr. Cardiol. Rep.* **2015**, *17* (12), 110. https://doi.org/10.1007/s11886-015-0666-9.

(16) Vigne, J.; Thackeray, J.; Essers, J.; Makowski, M.; Varasteh, Z.; Curaj, A.; Karlas, A.; Canet-Soulas, E.; Mulder, W.; Kiessling, F.; et al. Current and Emerging Preclinical Approaches for Imaging-Based Characterization of Atherosclerosis. *Mol. Imaging Biol.* **2018**, *20* (6), 869–887. https://doi.org/10.1007/s11307-018-1264-1.

(17) Rathod, K. S.; Hamshere, S. M.; Jones, D. A.; Mathur, A. Intravascular Ultrasound Versus Optical Coherence Tomography for Coronary Artery Imaging – Apples and Oranges? *Interv. Cardiol. Rev.* **2015**, *10* (1), 8–15. https://doi.org/10.15420/icr.2015.10.1.8.

(18) de Boer, S. P. M.; Brugaletta, S.; Garcia-Garcia, H. M.; Simsek, C.; Heo, J. H.; Lenzen, M. J.; Schultz, C.; Regar, E.; Zijlstra, F.; Boersma, E.; et al. Determinants of High Cardiovascular Risk in Relation to Plaque-Composition of a Non-Culprit Coronary Segment Visualized by near-Infrared Spectroscopy in Patients Undergoing Percutaneous Coronary Intervention. *Eur. Heart J.* **2014**, *35* (5), 282–289. https://doi.org/10.1093/eurheartj/eht378.

(19) Hammad, B.; Evans, N. R.; Rudd, J. H. F.; Tawakol, A. Molecular Imaging of Atherosclerosis with Integrated PET Imaging. *J. Nucl. Cardiol.* **2017**, *24* (3), 938–943. https://doi.org/10.1007/s12350-016-0766-y.

(20) Moghbel, M.; Al-Zaghal, A.; Werner, T. J.; Constantinescu, C. M.; Høilund-Carlsen, P. F.; Alavi, A. The Role of PET in Evaluating Atherosclerosis: A Critical Review. *Semin. Nucl. Med.* **2018**, *48* (6), 488–497. https://doi.org/10.1053/j.semnuclmed.2018.07.001.

(21) Meester, E. J.; Krenning, B. J.; de Swart, J.; Segbers, M.; Barrett, H. E.; Bernsen, M. R.; Van der Heiden, K.; de Jong, M. Perspectives on Small Animal Radionuclide Imaging; Considerations and Advances in Atherosclerosis. *Front. Med.* **2019**, *6*. https://doi.org/10.3389/fmed.2019.00039.

(22) Skagen, K.; Johnsrud, K.; Evensen, K.; Scott, H.; Krohg-Sørensen, K.; Reier-Nilsen, F.; Revheim, M.-E.; Fjeld, J. G.; Skjelland, M.; Russell, D. Carotid Plaque Inflammation Assessed with 18F-FDG PET/CT Is Higher in Symptomatic Compared with Asymptomatic Patients. *Int. J. Stroke* **2015**, *10* (5), 730–736. https://doi.org/10.1111/ijs.12430.

(23) Tawakol, A.; Migrino, R. Q.; Bashian, G. G.; Bedri, S.; Vermylen, D.; Cury, R. C.; Yates, D.; LaMuraglia, G. M.; Furie, K.; Houser, S.; et al. In Vivo 18F-Fluorodeoxyglucose Positron Emission Tomography Imaging Provides a Noninvasive Measure of Carotid Plaque Inflammation in Patients. *J. Am. Coll. Cardiol.* **2006**, *48* (9), 1818–1824. https://doi.org/10.1016/j.jacc.2006.05.076.

(24) Joshi, N. V.; Vesey, A. T.; Williams, M. C.; Shah, A. S. V.; Calvert, P. A.; Craighead, F. H. M.; Yeoh, S. E.; Wallace, W.; Salter, D.; Fletcher, A. M.; et al. 18F-Fluoride Positron Emission Tomography for Identification of Ruptured and High-Risk Coronary Atherosclerotic Plaques: A Prospective Clinical Trial. *The Lancet* **2014**, *383* (9918), 705–713. https://doi.org/10.1016/S0140-6736(13)61754-7.

(25) Rudd, J. H. F.; Narula, J.; Strauss, H. W.; Virmani, R.; Machac, J.; Klimas, M.; Tahara, N.; Fuster, V.; Warburton, E. A.; Fayad, Z. A.; et al. Imaging Atherosclerotic Plaque Inflammation by Fluorodeoxyglucose With Positron Emission Tomography. *J. Am. Coll. Cardiol.* **2010**, *55* (23), 2527–2535. https://doi.org/10.1016/j.jacc.2009.12.061.

(26) Emini Veseli, B.; Perrotta, P.; De Meyer, G. R. A.; Roth, L.; Van der Donckt, C.; Martinet, W.; De Meyer, G. R. Y. Animal Models of Atherosclerosis. *Eur. J. Pharmacol.* https://doi.org/10.1016/j.ejphar.2017.05.010.

(27) Van der Donckt, C.; Van Herck, J. L.; Schrijvers, D. M.; Vanhoutte, G.; Verhoye, M.; Blockx, I.; Van Der Linden, A.; Bauters, D.; Lijnen, H. R.; Sluimer, J. C.; et al. Elastin Fragmentation in Atherosclerotic Mice Leads to Intraplaque Neovascularization, Plaque Rupture, Myocardial Infarction, Stroke, and Sudden Death. *Eur. Heart J.* **2015**, *36* (17), 1049–1058. https://doi.org/10.1093/eurheartj/ehu041.

(28) Gee, A. D.; Bongarzone, S.; Wilson, A. A. Small Molecules as Radiopharmaceutical Vectors. In *Radiopharmaceutical Chemistry*; Lewis, J. S., Windhorst, A. D., Zeglis, B. M., Eds.; Springer International Publishing: Cham, 2019; pp 119–136. https://doi.org/10.1007/978-3-319-98947-1_7.

(29) Minchenko, O.; Opentanova, I.; Caro, J. Hypoxic Regulation of the 6-Phosphofructo-2-Kinase/Fructose-2,6-Bisphosphatase Gene Family (PFKFB-1–4) Expression in Vivo. *FEBS Lett.* **2003**, *554* (3), 264–270. https://doi.org/10.1016/S0014-5793(03)01179-7.

(30) Cao, Y.; Zhang, X.; Wang, L.; Yang, Q.; Ma, Q.; Xu, J.; Wang, J.; Kovacs, L.; Ayon, R. J.; Liu, Z.; et al. PFKFB3-Mediated Endothelial Glycolysis Promotes Pulmonary Hypertension. *Proc. Natl. Acad. Sci.* **2019**, *116* (27),

13394–13403. https://doi.org/10.1073/pnas.1821401116.

(31) Tissue expression of PFKFB3 - Summary - The Human Protein Atlas https://www.proteinatlas.org/ENSG00000170525-PFKFB3/tissue (accessed Feb 18, 2020).

(32) Position paper of the Cardiovascular Committee of the European Association of Nuclear Medicine (EANM) on PET imaging of atherosclerosis | SpringerLink https://link.springer.com/article/10.1007%2Fs00259-015-3259-3 (accessed Feb 5, 2019).

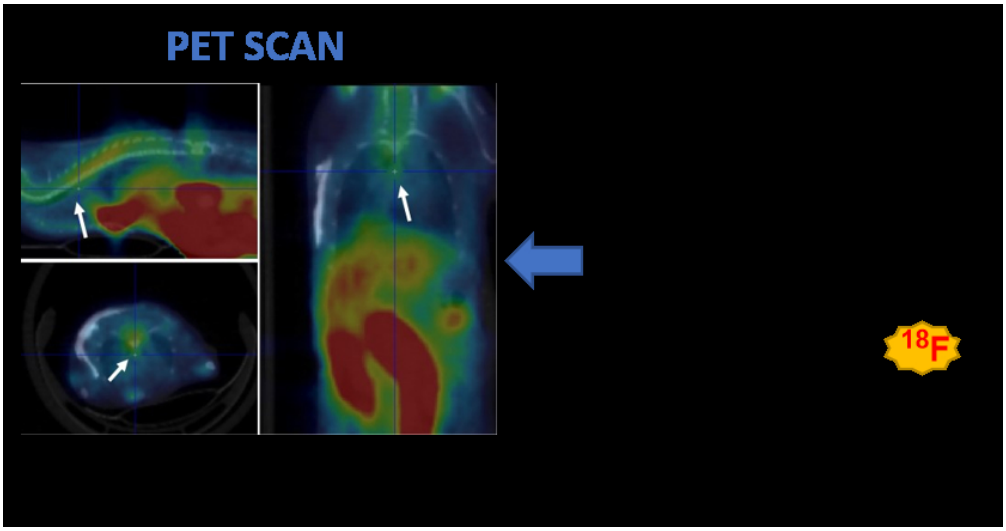

141x73mm (150 x 150 DPI)

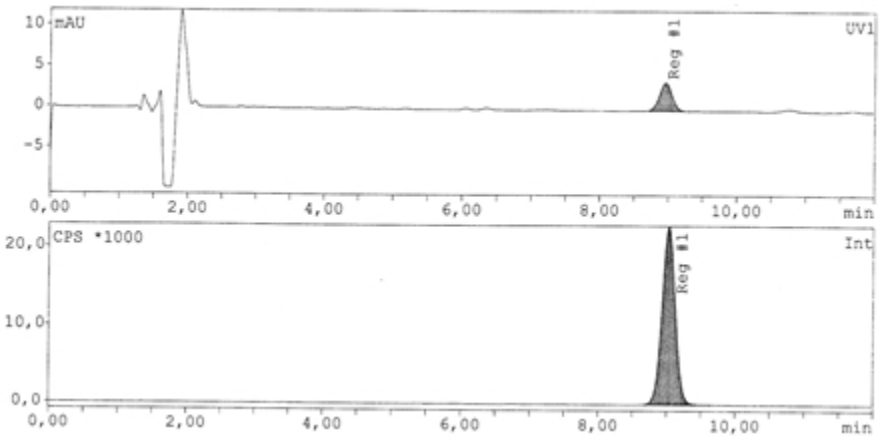

84x39mm (141 x 142 DPI)

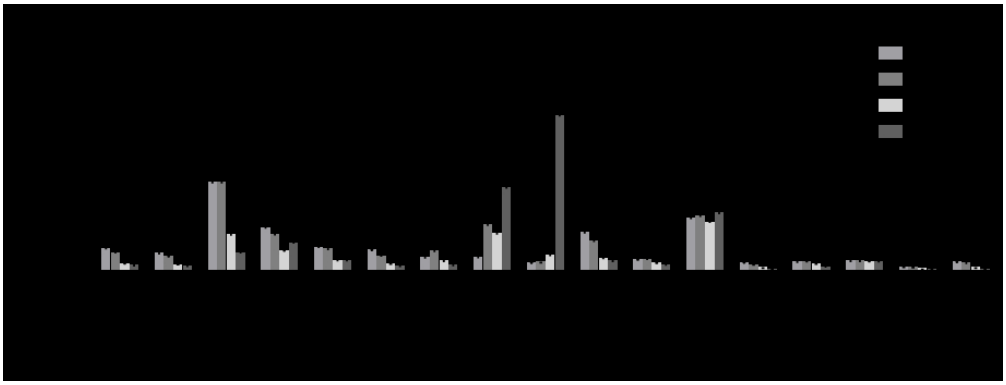

155x58mm (150 x 150 DPI)

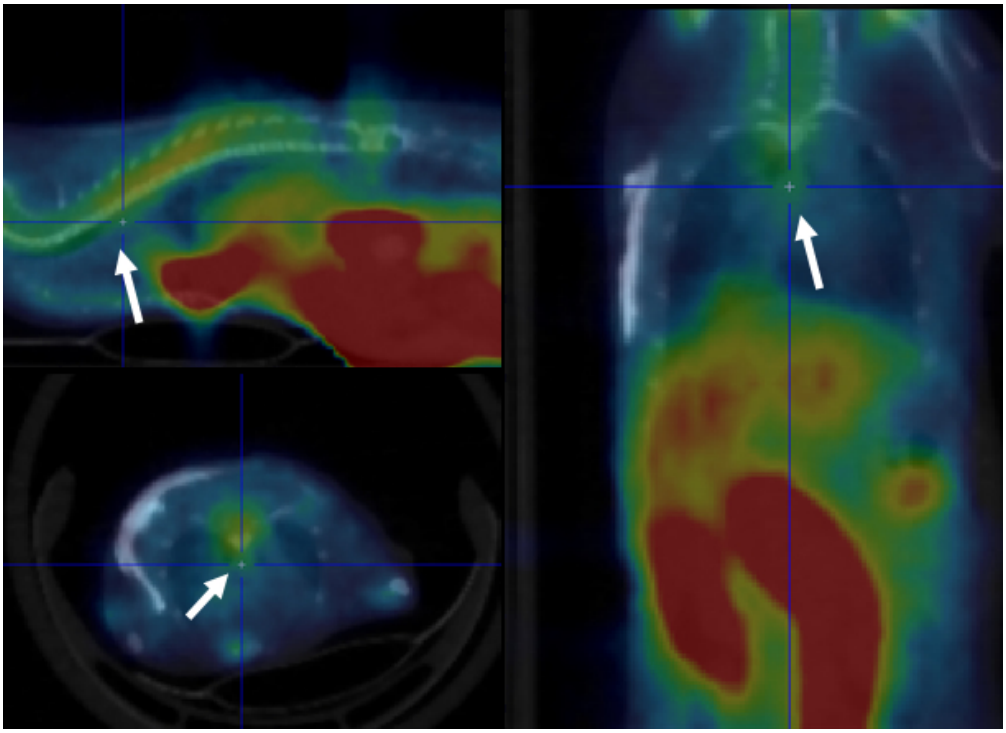

109x78mm (141 x 142 DPI)

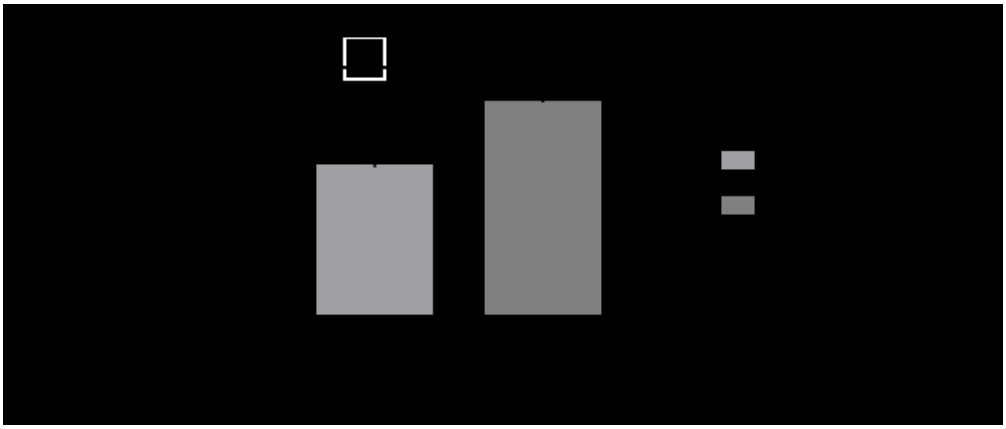

158x66mm (96 x 96 DPI)

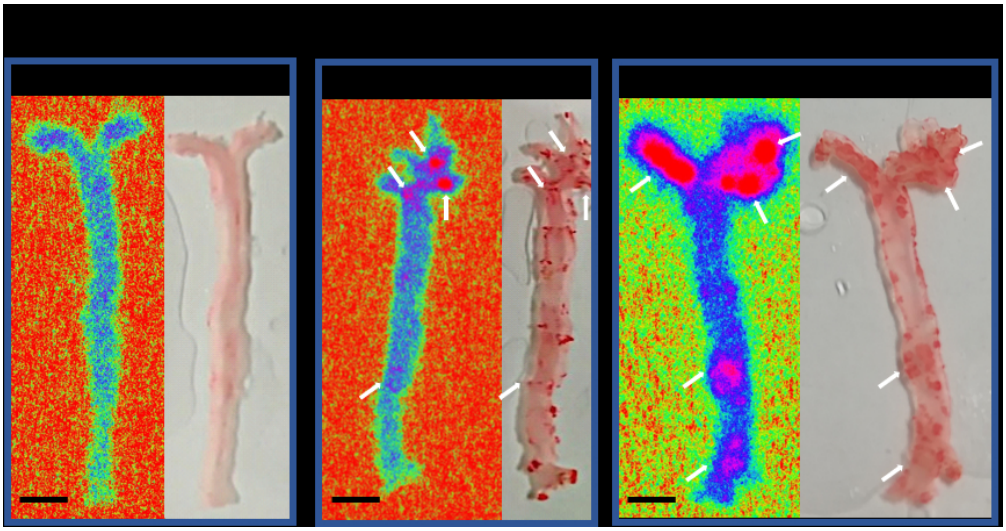

145x76mm (150 x 150 DPI)

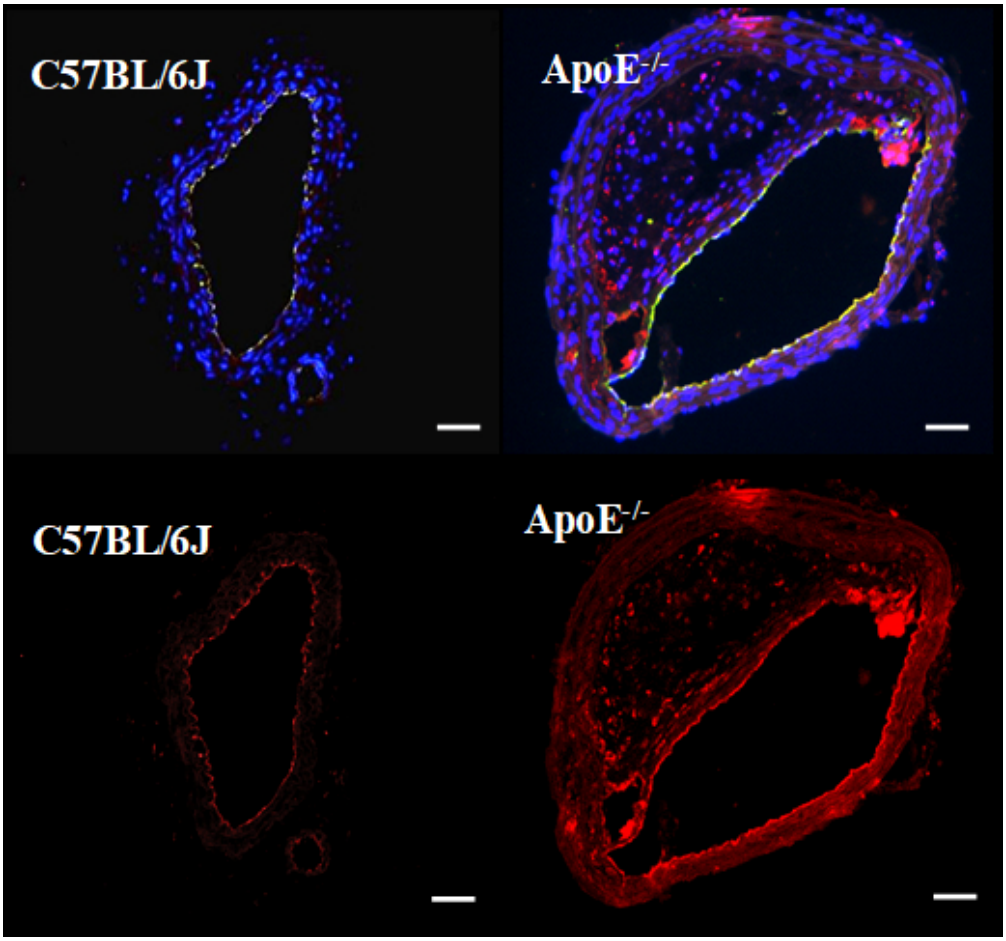

93x86mm (141 x 142 DPI)

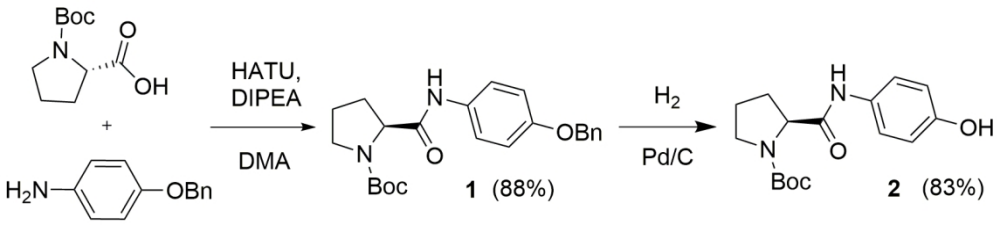

150x33mm (300 x 300 DPI)

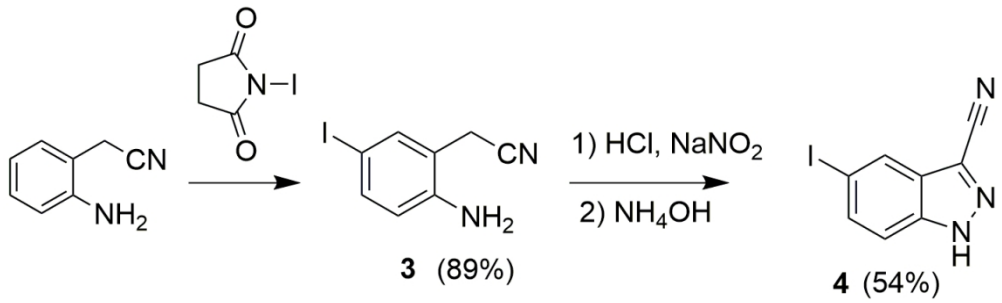

120x37mm (300 x 300 DPI)

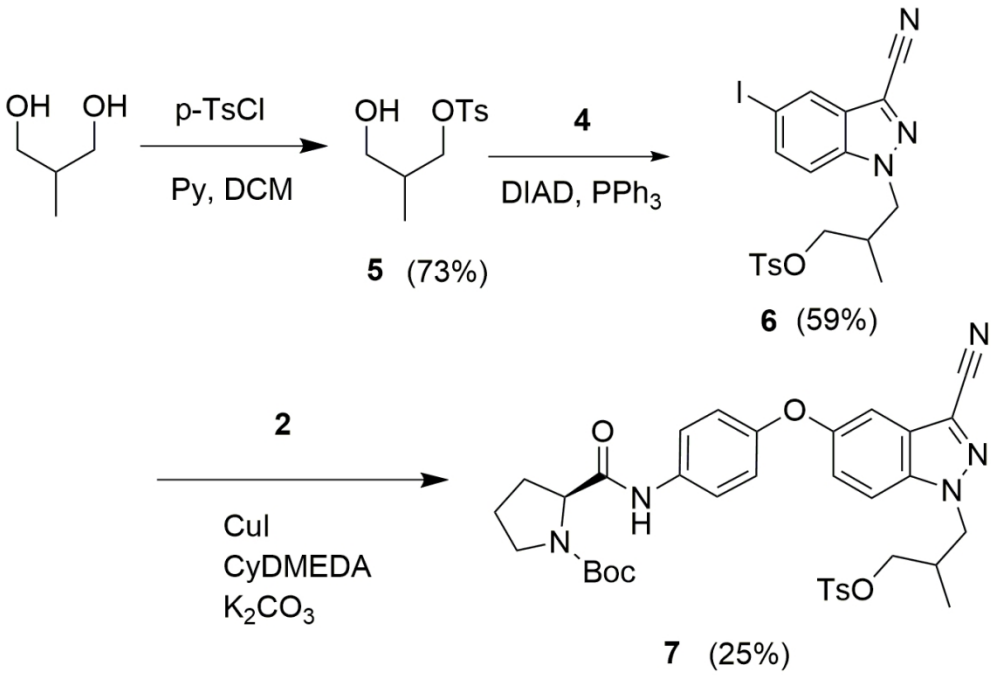

114x77mm (300 x 300 DPI)

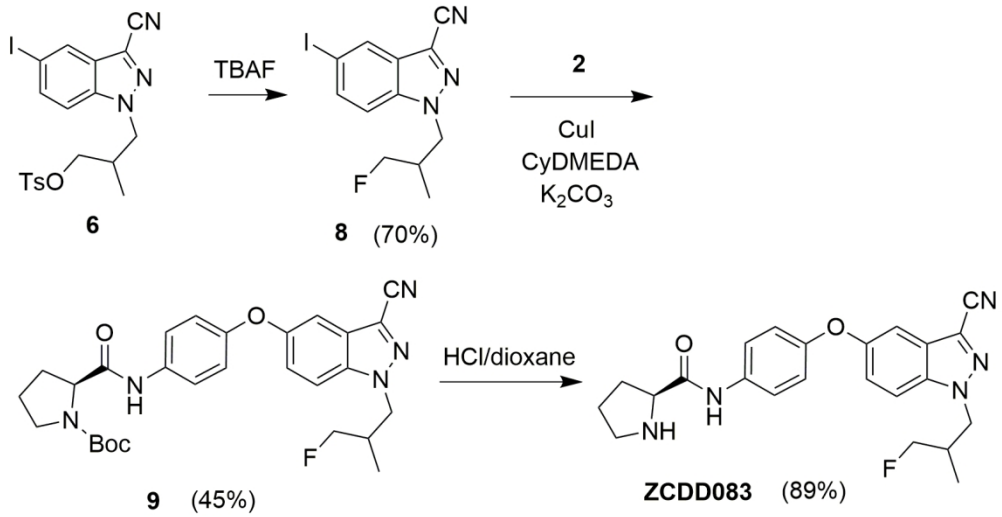

144x75mm (300 x 300 DPI)

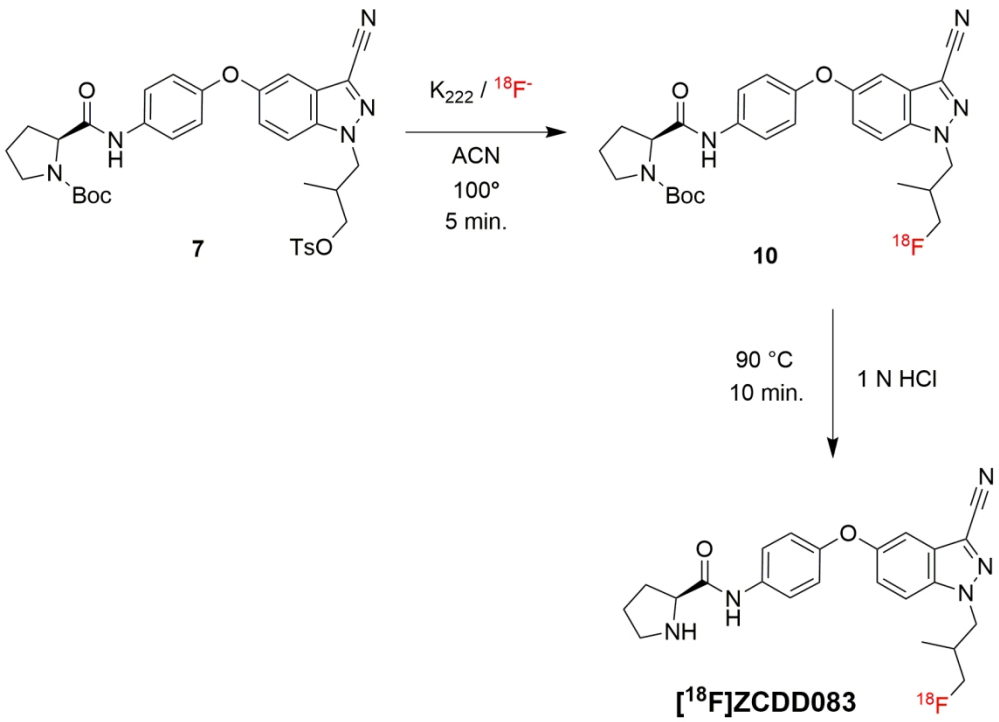

152x110mm (300 x 300 DPI)